Rotation rates of 36 decameter scale asteroids

Mehul Ghosal[a,*], Bryce Bolin[b], Robert Jedicke[a]

[a] *University of Hawaii*
[b] *Caltech*

Abstract

Asteroids larger than a few hundred meters in diameter exhibit an upper limit in their rotation rates at 2.2 hours because they are weakly bound rubble piles. The transition in that diameter range is thought to represent the boundary between monolithic asteroids and rubble piles, but there are as-yet few constraints on the tensile strength of decameter scale asteroids. We present lightcurves and rotation periods for two dozen small near Earth objects (NEOs) using sets of minute-long exposures from CFHT-Megacam and demonstrate a new rapid-response technique for extracting lightcurves of these small asteroids. We confirm the previously measured rotation periods for 2016 GE_1, 2016 EL_{157} and 2016 EN_{156}, report a dozen new periods, with the rest of our sample presenting ambiguous lightcurves. The $g-i$ and $r-i$ colors for most of the objects in our sample allow us to classify our asteroids into appropriate taxa.

Keywords: example, LaTeX, template

1. Introduction

Over the past two decades evidence has accumulated that large asteroids are conglomerates of smaller rocks held together by self-gravitation and weak mechanical forces. Colloquially, they are known as "rubble piles". The size range at which asteroids are more likely to be cohesive rocks rather than rubble piles lies in the decameter to hectameter range (Bottkejr et al., 2005). This paper presents a technique for the rapid determination of rotation rates of new small asteroids to probe the transition from rubble pile to monolith with observations of decameter scale NEOs.

Meteorite samples provide evidence that large planetesimals formed early in the solar system's proto-planetary disk from millimeter and centimeter scale pebbles. The largest of these objects grew into the giant planets Jupiter and Saturn and their subsequent migration fueled the scattering and mixing of the remaining material laying the basis of the asteroid populations we see now. (Izidoro et al., 2021) Large asteroids differentiated via heat of accumulation and later radiogenic heating, and then collisions fragmented these asteroids into smaller rocks. Evolved asteroids will fracture many times over their lifetimes until the fragments fall into the strength-dominated regime (Bottke et al., 2005).

We infer the tensile strength of asteroids by determining their rotation rates versus diameter (fig. 1). The faster an asteroid spins, the stronger it must be held together to avoid being torn apart by centripetal acceleration. Most asteroids larger than 200 m lie in the gravity-dominated regime and are primarily held together by self-gravity. Accurate photometric lightcurve analysis of thousands of asteroids suggest nearly all asteroids smaller than 60 m and nearly none larger than 170 m spin with periods faster than 2 hours (Statler et al., 2013). These observations imply that the strength regime changes in this size but not enough rotation rates have been measured at the smallest sizes to constrain the transition region and set a limit on these objects's tensile strength. The observational bias against small asteroids due to their faintness and short windows of observability limits the number of objects with reported rotation rates (fig. 1) motivating this study of decameter scale objects to determine their morphological properties.

Most asteroids larger than 150 meters rotate with periods longer than 2.2 hours (fig. 1). At that critical rotation rate centrifugal forces overcome the weak binding mechanical and electromagnetic forces holding the rubble together and break the asteroid apart. Some smaller-than-kilometer aggregates of rock are strong enough to withstand the rotational stresses (Statler et al., 2013) but most asteroids with diameters $D < 60$ m are rapid rotators. This indicates that some tensile strength provides enough bulk force to counteract fast rotation.

NEO dynamics are dominated by gravitational interactions, collisions, and solar radiation; the Yarkovsky–O'Keefe–Radzievskii–Paddack (YORP) effect acts to change the spin state of rotating asteroids due to scattering of solar radiation continuously adding or subtracting angular momentum. YORP-driven dynamics lead to spin obliquities oscillating between 0°, 90° or 180°, relative to the ecliptic, resulting in many spin cycles over the lifetime of an NEO (Statler et al., 2013). Low strength large asteroids spin-up to their rotational limit and break into smaller pieces and the cycle continues until the remaining fragments are monoliths strong enough to withstand disruption due to spin-up. YORP

*Corresponding author

Email addresses: mehul@hawaii.edu (Mehul Ghosal), bbolin@caltech.edu (Bryce Bolin), jedicke@hawaii.edu (Robert Jedicke)

can then drive the monoliths to have spin obliquities close to parallel or orthogonal to the ecliptic, but it can also force them into chaotic rotation states (Hergenrother and Whiteley, 2011).

Near Earth asteroids (NEA), those with perihelia $q \leq 1.3$ au, provide a means to characterize smaller asteroids than those that are detectable in the main belt because they can approach much closer to Earth. Even so, NEAs less than 150 meters in diameter, with absolute magnitudes $H \gtrsim 21.5$, are exceptionally difficult to characterize because they are often faint, have fast apparent rates of motion, visible for only short periods of time, and their orbits can not be propagated to their next apparition for extensive followup. Thus, the discovery apparition is often the best opportunity for characterization but rapid response to targets of opportunity is not usually possible.

Wide-field surveys like PANSTARRS, CSS, ZTF and ATLAS, are discovering new NEOs on a daily basis but the rate of follow-up characterization for the small asteroids has not been able to keep up. Capturing rotation rates of small NEOs normally demands fast-readout times and large aperture telescopes. Amateur astronomers contributing to the NEO confirmation effort generally cannot achieve the signal-to-noise necessary to determine the rotation periods of these faint, fast moving asteroids, but professional telescopes require months of notice to reserve time, and their large cameras have long readout times, making it difficult to determine the rotation rates of rapid rotators. The technique described in Section 2 is motivated by the need for rapid response systems to characterize these objects.

Decameter-scale asteroids are relevant to planetary defense because they are the most common, if not the most dangerous, class of impactor that can cause surface damage (Brown et al., 2013). These Tunguska-like asteroids are predicted to impact once per hundred years and have the potential to wipe out cities and countries . Rotation rate, tensile strength, and size are key parameters in the impactors's fragmentation and fireball, essential to estimating the damage delivered by impactors to the Earth's surface (Whe).

Similarly, target selection by future asteroid mining companies for in-situ resource utilization (ISRU) will prioritize small asteroids with low rotation rates and those in simple spin states The advantage for ISRU selection in the NEO population is access to many asteroids with low Δv roundtrip (Jedicke et al., 2022). Thousands of small NEOs could serve as ISRU targets but we know of only 5% (Jedicke et al., 2018). Only a small fraction of this population have any physical characterization at all. Thus, science, planetary defense, and commercial space activity will all benefit from rapid response to new asteroid detections and the measurement of physical properties derived from these observations.

2. Method

We take advantage of CFHT's automatic queuing service to demonstrate the rapid response capability needed for follow up on NEO characterization. We artificially trail an asteroid's image along a CCD column or row such that the asteroid lightcurve is obtained as flux as a function of position along the trail. This negates the concern for CCD readout time, allowing us to obtain lightcurves of rapid rotators.

2.1. Observations

Observations of 36 decameter-scale asteroids were acquired with CFHT MegaCam (Appendix A) in late 2015 and early 2016 for recently discovered NEOs near in time to their closest approach to Earth. CFHT's queue scheduling service provides the flexibility to aquire images on short notice for these targets of opportunity. The asteroids were selected based on their absolute magnitude ($H > 26$), apparent brightness, and rate of motion (table **??**). We calculated the non-sidereal tracking rate required to trail the asteroid's image along a CCD row or column (fig. 2) during the exposure at a magnitude-dependent rate in an attempt to control the signal-to-noise ration (SNR). The realized asteroid trails range from 30 to 150 pixels in length with shorter trails corresponding to fainter asteroids. The stars in the field are trailed in a different orientation corresponding to the combined sidereal motion of the sky and tracking of the telescope.

Each asteroid was imaged six times in 60 second exposures. The sequence of exposures over only 12 minutes (including readout time) limits our ability to determine the rotation state and shape of the asteroids because we do not observe many rotation periods and observe the asteroid at essentially one sub-Earth latitude (Kwiatkowski et al., 2021).

Two exposure were taken in each of the g, r, and i bands with the expectation that we could determine the asteroid's color after calibrating the images. Color can be used to classify asteroids into taxonomic groups that are correlated with their bulk composition which could be related to their tensile strengths and their maximum rotation rates.

Images were pre-processed by Elixir from CFHT (Magnier and Cuillandre, 2004). Elixir applied overscan, bias, flats, and dark corrections to the images, removing fringe structures.

2.2. Lightcurve reduction

Each image was visually inspected to identify the asteroid trail and measure the approximate coordinates of its centroid. Three of the 36 asteroids were not identified in any of their exposures.

`SExtractor`Bertin? was used to identify sources on the same MegaCam chip as the asteroid and then each source was fit to an idealized trail (Vereš et al., 2012), a Gaussian point spread function convoluted with a straight line:

$$f(x,y) = B + \frac{\Phi}{2\sigma L\sqrt{2\pi}} \exp\left(-\frac{((x-x_0)\sin\phi_0 + (y-y_0)\cos\phi_0)^2}{2\sigma^2}\right) \left[\operatorname{erf}\left(\frac{(x-x_0)\cos\phi_0 + (y-y_0)\sin\phi_0 + L/2}{\sigma\sqrt{2}}\right) - \operatorname{erf}\left(\frac{(x-x_0)\cos\phi_0 + (y-y_0)\sin\phi_0 - L/2}{\sigma\sqrt{2}}\right)\right] \tag{1}$$

where (x_0, y_0) represent the pixel coordinates of the trail's centroid, ϕ_0 is the angle made by the trail realtive to the positive

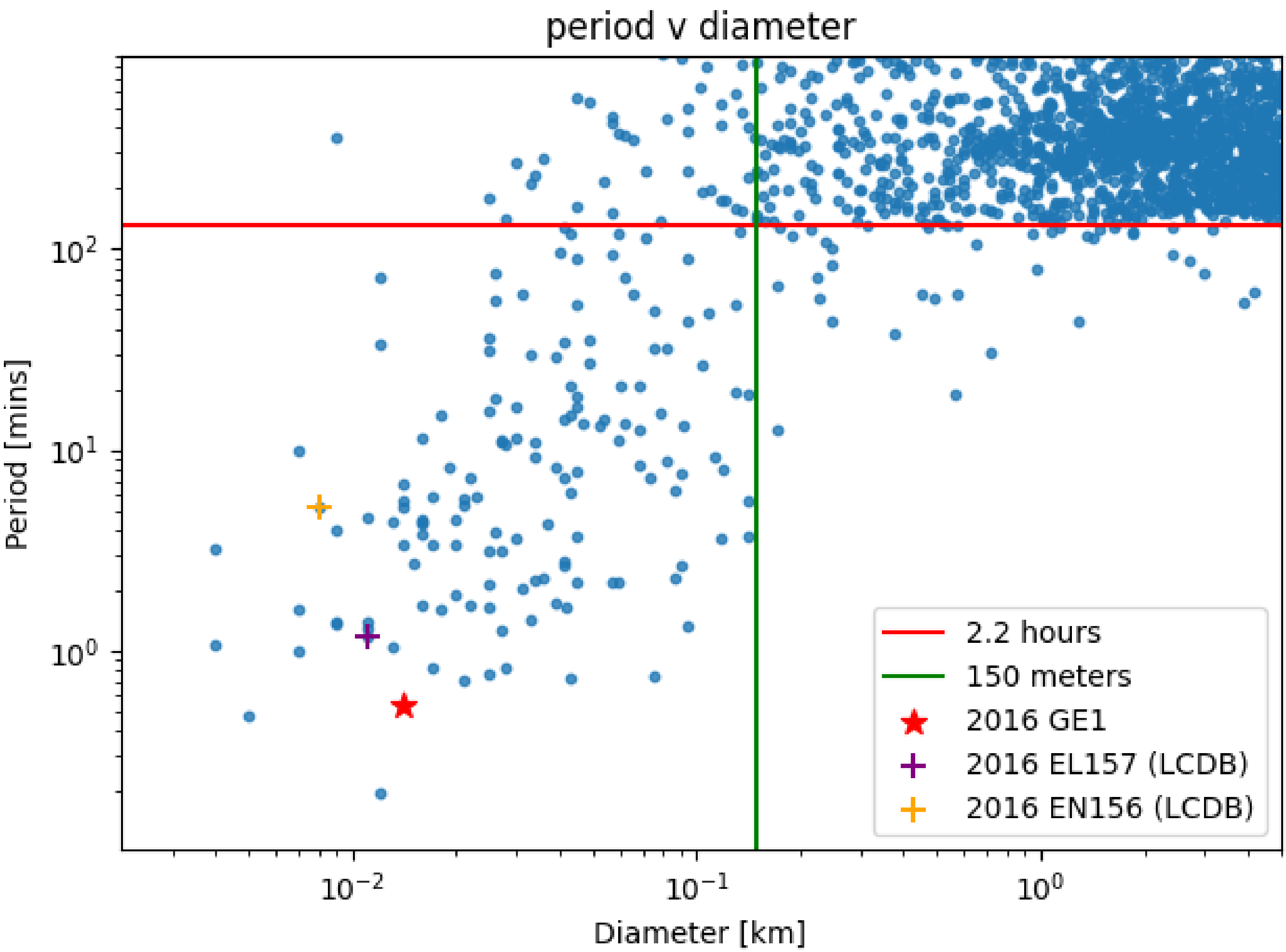

Figure 1: Period versus diameter for asteroids with well-measured periods (U=2* or 3*) from the Asteroid Lightcurve Database (LCDB, Bundle V4.0). The red horizontal line at a rotation period of 2.2 h and the green vertical line at a diameter of 150 m highlight the disparity in rotation rates between small and large asteroids.

x-axis, L is the trail length, σ is the standard deviation of the Gaussian representing the point spread function (PSF), Φ is the total flux in the trail, and B represents the background sky. The fit was obtained with `Scipy.optimize.curve_fit` which also provides the 1-σ uncertainties on the fitted parameters.

The fitted trail is clearly idealized (fig. 2) but still provides a consistent means of defining the trail start and ending points and the trail width necessary for reducing the light curve. The center of the real trail varies from row to row as a consequence of the imperfect tracking of the telescope and time-varying and localized seeing but `curve_fit` returns the row-averaged centroid.

Prior to extracting lightcurves from the asteroid trails, each frame was rotated by $-\phi_0^\circ$ using the flux-conserving routine provided by `Scipy.ndimage.rotate` resulting in asteroid trails exactly aligned with the CCD columns. ϕ_0 was not 0° or 90° because the orbits of the NEOs at the time of observation were not well constrained, so our calculation of the non-sidereal tracking rates could introduce a small error resulting in an off-axis trail.

Once the trails were oriented along CCD columns the row number is linearly correlated with time and the physical rotation of the asteroid will result in a time-varying flux along the rows if the asteroid is rotating and not spherical or has surface albedo variations. While the fitted trail parameters are real numbers our light curve reduction is integer pixel based and we define the integer number of pixels in one full-width-at-half-maximum (`FWHM`) of the PSF as $n_w = \mathtt{ceil}(2.355\ \sigma)$. The fitted trail's endpoints are given by

$$(x_1, y_1) = (x_0, y_0 + L/2) \quad (2)$$
$$(x_2, y_2) = (x_0, y_0 - L/2) \quad (3)$$

but we truncate the trail on each end by n_w pixels to eliminate edge effects at the beginning and end of the exposure. Thus, the effective trail length is $L = L_0 - 2n_w$ pixels.

Letting $i_n = \mathrm{int}(x_n)$ represent the column/pixel number containing the position x_n and $j_n = \mathrm{int}(y_n)$ represent the row number containing the position y_n, the integer pixel bounds for the asteroid's signal are:

$$\begin{aligned} i_{min} &= \texttt{floor}(\ y_0 - L/2\ ) \\ i_{max} &= \texttt{ceil}(\ y_0 + L/2\ ) \\ j_{min} &= \texttt{floor}(\ x_0 - n_w\ ) \\ j_{max} &= \texttt{ceil}(\ x_0 + n_w\ ) \end{aligned} \tag{4}$$

The total flux in each row n through m inclusive is:

$$F_j = \sum_{j=m}^{n} \sum_{i=i_{min}}^{i_{max}} F_{ij} \tag{5}$$

where F_{ij} is the flux in pixel (i, j). We integrate across many columns to capture most of the flux of the trail and compensate for non-linear trailing due to drive and seeing irregularities (fig. 2).

The contribution of the sky background to the asteroid flux is calculated using a set of pixels adjacent to the streak. The bounds in i are identical to those in eq. 4 but the bounds in j are:

$$\begin{aligned} j_{-min} &= j_0 - n_w \\ j_{-max} &= j_0 - n_{sky} \\ j_{+min} &= j_0 + n_w \\ j_{+max} &= j_0 + n_{sky} \end{aligned} \tag{6}$$

where $n_{sky} = 4\ n_w$ and the $-$ and $+$ subscripts denote the sky region left and right of the trail, respectively. The total number of sky pixels is then $N_{sky} = 2(n_{sky} - n_w)$ The total flux in the defined sky background region in row j bracketing the asteroid trail is:

$$F_{sky,j} = \sum_{i=i_{-min}}^{i_{-max}} F_{ij} + \sum_{i=i_{+min}}^{i_{+max}} F_{ij}. \tag{7}$$

The average background flux per pixel in the region surrounding, and presumably beneath, the trail is then $\bar{F}_{sky,j} = F_{sky,j}/N_{sky}$. Finally, the background-corrected signal in the trail is:

$$S_j = F_j - N_{sky}\ \bar{F}_{sky,i} \tag{8}$$

2.3. Star Lightcurves

The next step in the process is to correct the lightcurve for sky transparency and/or telescope drive irregularities.

`SExtractor` identified sources on the chip including the star trails and provides and estimate of each source's centroid and pixel bounds. We fit the Vereš et al. (2012) trail model (eq. 1) using the `SExtractor` output as the starting values and generated lightcurves for every source in the field in the same manner as described for the asteroids (§2.2).

All of the stars in the field trail at the same rate and direction so they should have consistent lengths and angles on each chip. Thus, for the lightcurve correction, we select stars with fitted parameters (s, L, a) that are closer than 2 σ from the mean of all values on the chip. To ensure that the stars that are used for the lightcurve correction experience the same sky conditions as the asteroid we select the 10 best ($n_{star} = 10$) star trails with the smallest on-chip distance to the asteroid trail's centroid and that also have a χ^2/DOF residual of $< X$ with respect to eq. 1. The cut on the fit residual is a measure of the quality of the star trail.

As the star and asteroid trails are different lengths on the chip, we re-bin the longer of the two trails to the length of the shorter in a flux conserving binning. To generate this new binned lightcurve, we start by defining the new bin length in pixels as $N_{sum} = L_{star}/L_{ast}$ (assuming the star trails are longer than the asteroid). Each binned value is a fractional combination of the adjacent equivalent rows in the longer lightcurve.

To create a master star lightcurve, for each j, we take the average across all lightcurves:

$$\bar{F}_j = \sum_{n_{star}=1}^{10} S_{binned,i',N_{lc}}/10 \tag{9}$$

where N_{lc} spans from 1 to 10, representing each of the ten stars selected. Normalizing this median lightcurve to one, we now have a measure of the sky transparency as a function of time over the exposure length of the frame. We divide our trailed asteroid lightcurve by this normalized, median star lightcurve. This will remove any trends that affect regions on the CCD near the asteroid trail, giving us a more accurate picture of the asteroid's dynamics.

2.4. Error Analysis

The error on the background subtracted flux as a function of row number is :

$$\sigma_j^2 = \frac{F_j}{G} + n_w\left(\frac{\bar{F}_{sky,j}}{G} + R^2\right) + n_w^2\sigma_{sky}^2 \tag{10}$$

where G is the CCD gain, the number of CCD 'counts' per e^-, R is the read noise of the electronics in e^-/pixel, and $\sigma_{sky} = \sqrt{F_{sky}}/N_{sky}$.

For the combined average star lightcurve, the error on each value is

$$\sigma_{\bar{F}_j}^2 = \sum_{n=1}^{10} \sigma_{j,n}^2 \tag{11}$$

where N ranges from 1 to 10, indexing the best 10 stars.

We do not need to calibrate an absolute magnitude to obtain the colors of the asteroid. In fact, priliminary attempts to calibrate increased uncertainties on our lightcurves. Instead, we can normalize the lightcurves in a sequence for one asteroid to zero, where the normalization factors are consistent within a filter. We use these normalization factors to calculate the $g - i$ and $i - r$ colors of our asteroids. After appropriate calibration and normalization, we can stitch the lightcurves from each exposure together in chronological order.

2.5. Period determination

We use the Lomb-Scargle periodogram to determine the dominant frequencies in the corrected lightcurves. The Lomb-Scargle periodogram is preferred to a Fourier transform because

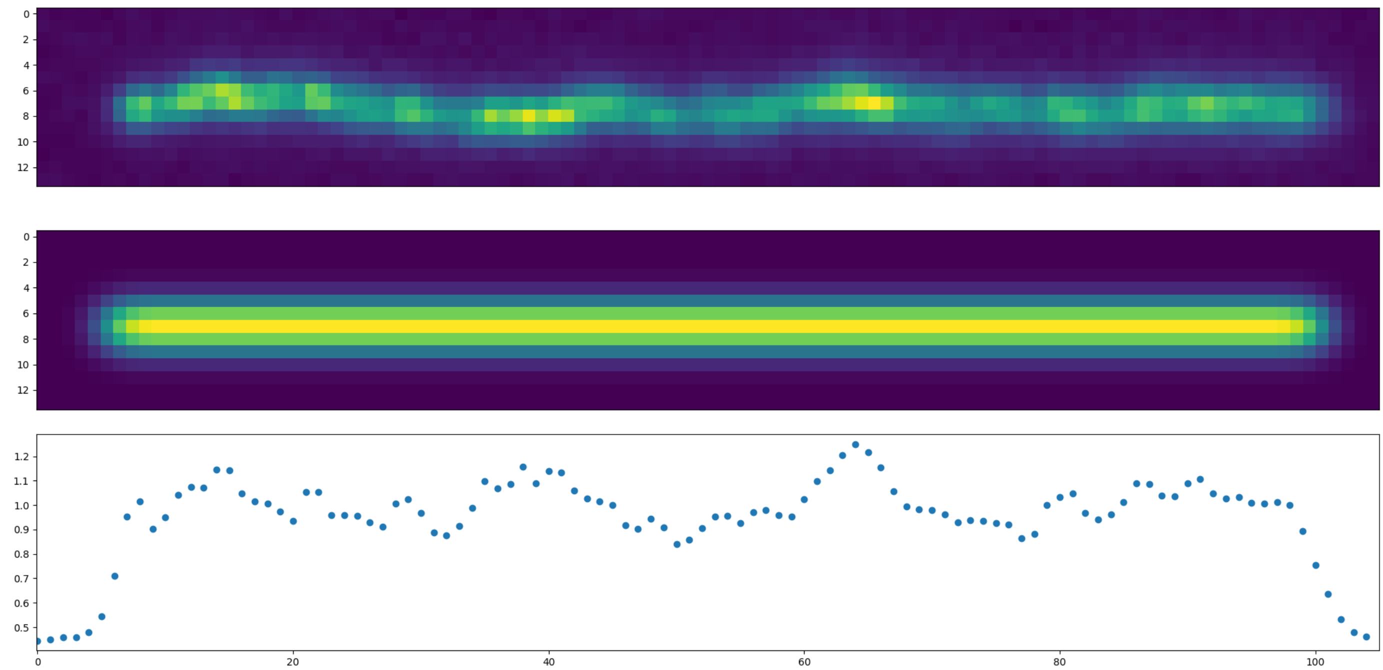

Figure 2: (top) Asteroid 2016 GE_1 trail from 4 April 2016 rotated by 90°. (middle) The same trail as realized from the Vereš et al. (2012) trail fit (eq. 1). (bottom) The sum of the flux in each column versus column number normalized by the median of the lightcurve. The flux has not yet been corrected for sky background and transparency. The ends of the lightcurve fall to zero because they sample the background sky.

of its optimization for sparsely sampled data as in our use of the stitched lightcurves. A Fourier transform would detect the sparsity of the lightcurve as the dominant mode instead of the lightcurve variation due to rotation.

3. Results & Discussion

Of the 36 asteroids planned for observations, we identified the asteroid trail in 28 of the image sequences. These sequences are composed of 2 60 second exposures each in g, r, and i filters from MegaCam, so gaps in our lightcurve correspond to a combination of CCD readout time and filter changes.

Three targets (2016 GE_1, 2016 EL_{157}, and 2016 EN_{156}) have known rotation rates reported in the LCDB.

3.1. 2016 GE_1

The asteroid 2016 GE_1 proved to be an excellent target to prove this methodology. This asteroid was well suited to our methodology because of its known 33.4 second rotation period and large amplitude of $\sim$ 0.6 mag. (Warner et al., 2009). Its lightcurve is obvious even from a single image (fig. **??** b), and its Lomb-Scargle (LS) periodogram from that exposure exhibits a significant peak at $P = 17.2$ s, half of the rotation period, as expected (**?**). The periodogram is restricted to the range from one second to one quarter of the time-range of all the exposures. We restrict the shortest rotation periods because we are insensitive to periods shorter than **XXX** due to binning in rows along the trail. The longest rotation period we can measure is assumed to be one quarter of the time range in order that we capture four full periods of rotation. Figure **??** then shows the time-series folded on itself at double the aforementioned peak. We double the peak to extract the dual peaks expected from a rotating triaxial asteroid. We find a rotation period of 34.3 s, differing by $<3\%$ from the LCDB's reported value of 33.4 s. The lightcurve amplitude is 0.6 mag from crest to trough. This agreement between our presented method and established works demonstrates our ability to extract rotation rates from a minute of exposure.

The periodogram calculated from the combined lightcurves is much messier. The first features of interest are the two peaks at $P = 110$ s and $P = 140$ s, which correspond to aliasing affects due to timing between exposures and filter changes. We currently have no explanation as to why the periodogram steadily increases with increasing period. Zooming into the periodogram, we can identify two more interesting peaks at $P = 15$ s and $P = 18$ s in Figure 5. This is closer to what we expect, and we show the entire sequence folded on $P = 35.1$ s, differing by 5%. Based on the normalization factors, 2016 GE_1 has a $g - i = .230$ and and $r - i = -.15$, indicating a slightly red asteroid, consistent with an S-type.

3.2. 2016 EV_{84}

Asteroid 2016 EV_{84} shows another excellent lightcurve. Again, we first present a lightcurve derived from a single 60 second exposure in Fig **??**. Fig **??** cuts out the noise of the periodogram found for periods less than one second, with only one significant peak at 28.6 seconds. Figure **??** next shows the stitched lightcurve folded on double this peak, with an ampli-

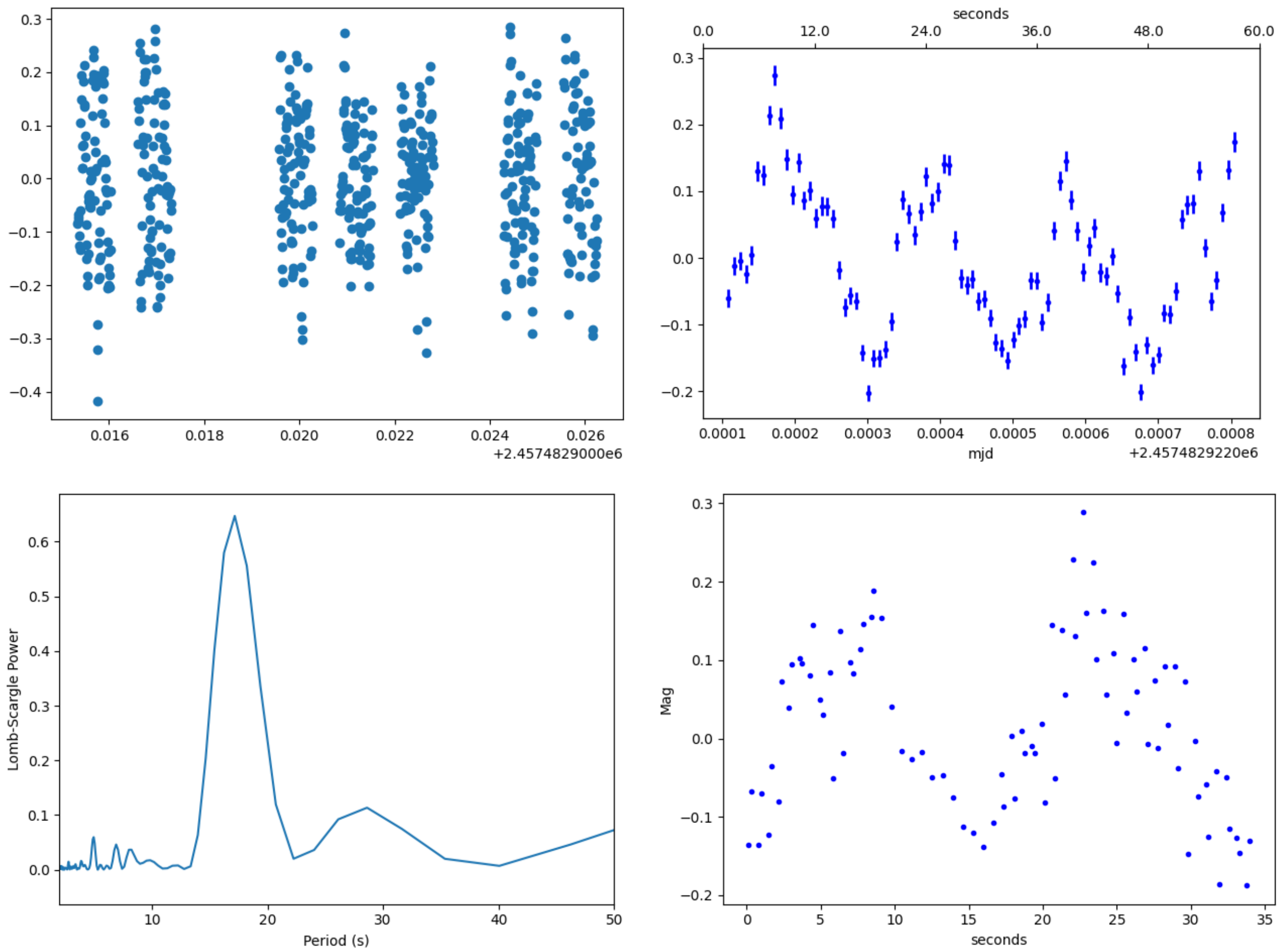

Figure 3: (a) Apparent magnitude of 2016 GE$_1$ over the course of seven exposures, 2 in g, 3 in r, and then 2 in i. The mean magnitude in each exposure is normalized to zero. (b) Detail of the same object's lightcurve in the from panel a. (c) Lomb-Scargle periodogram of the timeseries lightcurve presented in panel b. The dominant period is $P = 17.2$ s. (d) Folded lightcurve on double the dominant period from panel c. *i.e.* 34.4 s

tude of .4 mag. 2016 EV$_{84}$ is also an S type asteroid, indicated by $g - i = .65$ and $r - i = .20$.

Appendix A. Observations summary

See table Appendix A.

Acknowledgement

- Mehul Ghosal acknowledges support from Research Experience for Undergraduate program at the Institute for Astronomy, University of Hawaii-Manoa funded through NSF grant #2050710 and the Institute for Astronomy for their hospitality during the course of this project.

- This work is based on observations obtained with MegaPrime/MegaCam, a joint project of CFHT and CEA/DAPNIA, at the Canada-France-Hawaii Telescope (CFHT) which is operated by the National Research Council (NRC) of Canada, the Institut National des Science de l'Univers of the Centre National de la Recherche Scientifique (CNRS) of France, and the University of Hawaii. The observations at the Canada-France-Hawaii Telescope were performed with care and respect from the summit of Maunakea which is a significant cultural and historic site.

Appendix A.1. Software

- JPL Horizons, accessed via astroquery, through which asteroid ephemerides were obtained.

- SExtractor 2.25.0 for detecting sources on our images.

- Python 3.10.5, in which all analysis code was writen, using the following publically available packages: `numpy==1.21.5`, `matplotlib==3.5.1`, `astropy==5.0`, and `scipy==1.7.3`.

References

, .

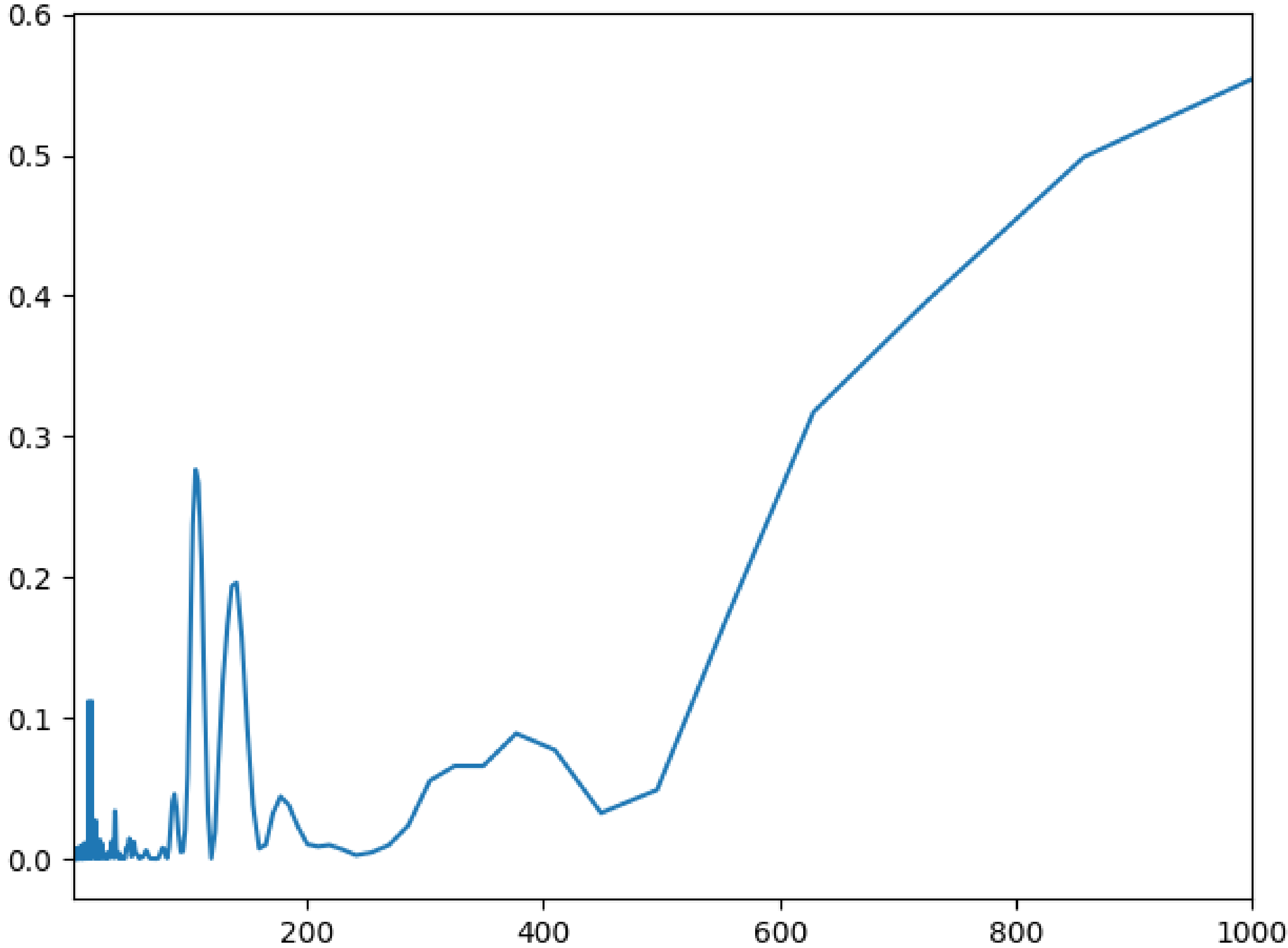

Figure 4: Lomb-Scargle periodogram from the stitched lightcurve sequence of 2016 GE_1.

Bottke, W.F., Durda, D.D., Nesvorný, D., Jedicke, R., Morbidelli, A., Vokrouhlický, D., Levison, H.F., 2005. Linking the collisional history of the main asteroid belt to its dynamical excitation and depletion. Icarus 179, 63–94.

Bottkejr, W., Durda, D., Nesvorny, D., Jedicke, R., Morbidelli, A., Vokrouhlicky, D., Levison, H., 2005. The fossilized size distribution of the main asteroid belt. Icarus 175, 111–140.

Brown, P.G., Assink, J.D., Astiz, L., Blaauw, R., Boslough, M.B., Borovička, J., Brachet, N., Brown, D., Campbell-Brown, M., Ceranna, L., Cooke, W., de Groot-Hedlin, C., Drob, D.P., Edwards, W., Evers, L.G., Garces, M., Gill, J., Hedlin, M., Kingery, A., Laske, G., Le Pichon, A., Mialle, P., Moser, D.E., Saffer, A., Silber, E., Smets, P., Spalding, R.E., Spurný, P., Tagliaferri, E., Uren, D., Weryk, R.J., Whitaker, R., Krzeminski, Z., 2013. A 500-kiloton airburst over Chelyabinsk and an enhanced hazard from small impactors. Nature 503, 238–241.

Hergenrother, C.W., Whiteley, R.J., 2011. A survey of small fast rotating asteroids among the near-Earth asteroid population. Icarus 214, 194–209.

Izidoro, A., Bitsch, B., Raymond, S.N., Johansen, A., Morbidelli, A., Lambrechts, M., Jacobson, S.A., 2021. Formation of planetary systems by pebble accretion and migration. Hot super-Earth systems from breaking compact resonant chains. A&A 650, A152. 1902.08772.

Jedicke, R., Hermosin, P., Sercel, J., Centuori, S., Sciarra, M., Cano, Á., Peterson, C., 2022. Optimized continuous-thrust round-trip trajectories to ultra-low Δv ISRU targets. Planet. Space Sci. 211, 105407.

Jedicke, R., Sercel, J., Gillis-Davis, J., Morenz, K.J., Gertsch, L., 2018. Availability and delta-v requirements for delivering water extracted from near-Earth objects to cis-lunar space. Planet. Space Sci. 159, 28–42.

Kwiatkowski, T., Koleńczuk, P., Kryszczyńska, A., Oszkiewicz, D., Kamiński, K., Kamińska, M.K., Troianskyi, V., Skiff, B., Moskowitz, N., Kashuba, V., Kim, M.J., Kim, T., Mottola, S., Santana-Ros, T., Kluwak, T., Buzzi, L., Bacci, P., Birtwhistle, P., Miles, R., Chatelain, J., 2021. Photometry and model of near-earth asteroid 2021 dw1 from one apparition. Astronomy & Astrophysics 656, A126.

Magnier, E.A., Cuillandre, J.C., 2004. The Elixir System: Data Characterization and Calibration at the Canada-France-Hawaii Telescope. PASP 116, 449–464.

Statler, T.S., Cotto-Figueroa, D., Riethmiller, D.A., Sweeney, K.M., 2013. Size matters: The rotation rates of small near-Earth asteroids. Icarus 225, 141–155.

Vereš, P., Jedicke, R., Denneau, L., Wainscoat, R., Holman, M.J., Lin, H., 2012. Improved Asteroid Astrometry and Photometry with Trail Fitting. PASP .

Warner, B.D., Harris, A.W., Pravec, P., 2009. The asteroid lightcurve database. Icarus 202, 134–146.

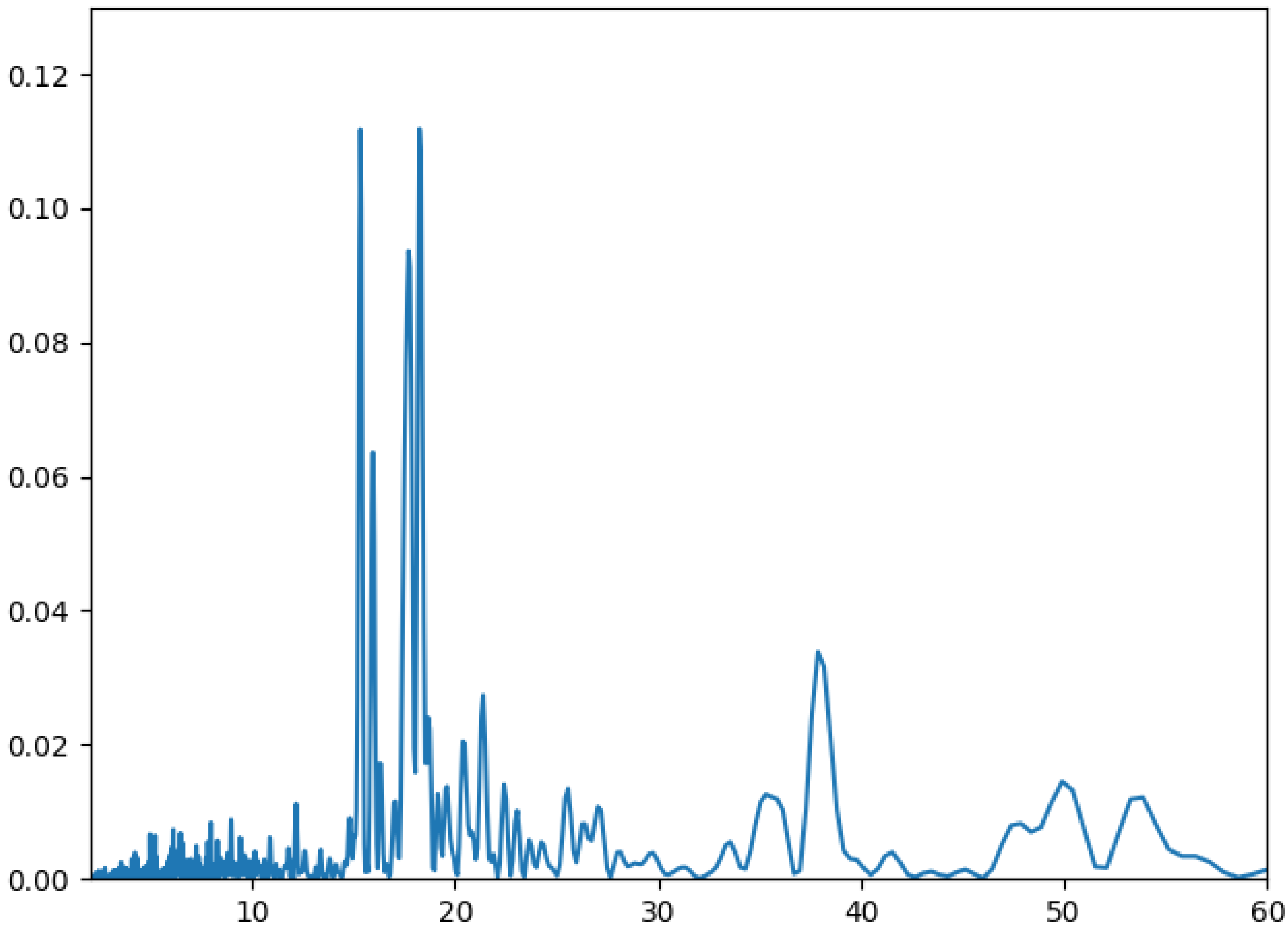

Figure 5: Same periodogram as displayed in Figure 4, but cropped into the region of interest: $P < 60\,\mathrm{s}$. The two distinct peaks occur at $P = 15.4\,\mathrm{s}$ and $P = 18.3\,\mathrm{s}$.

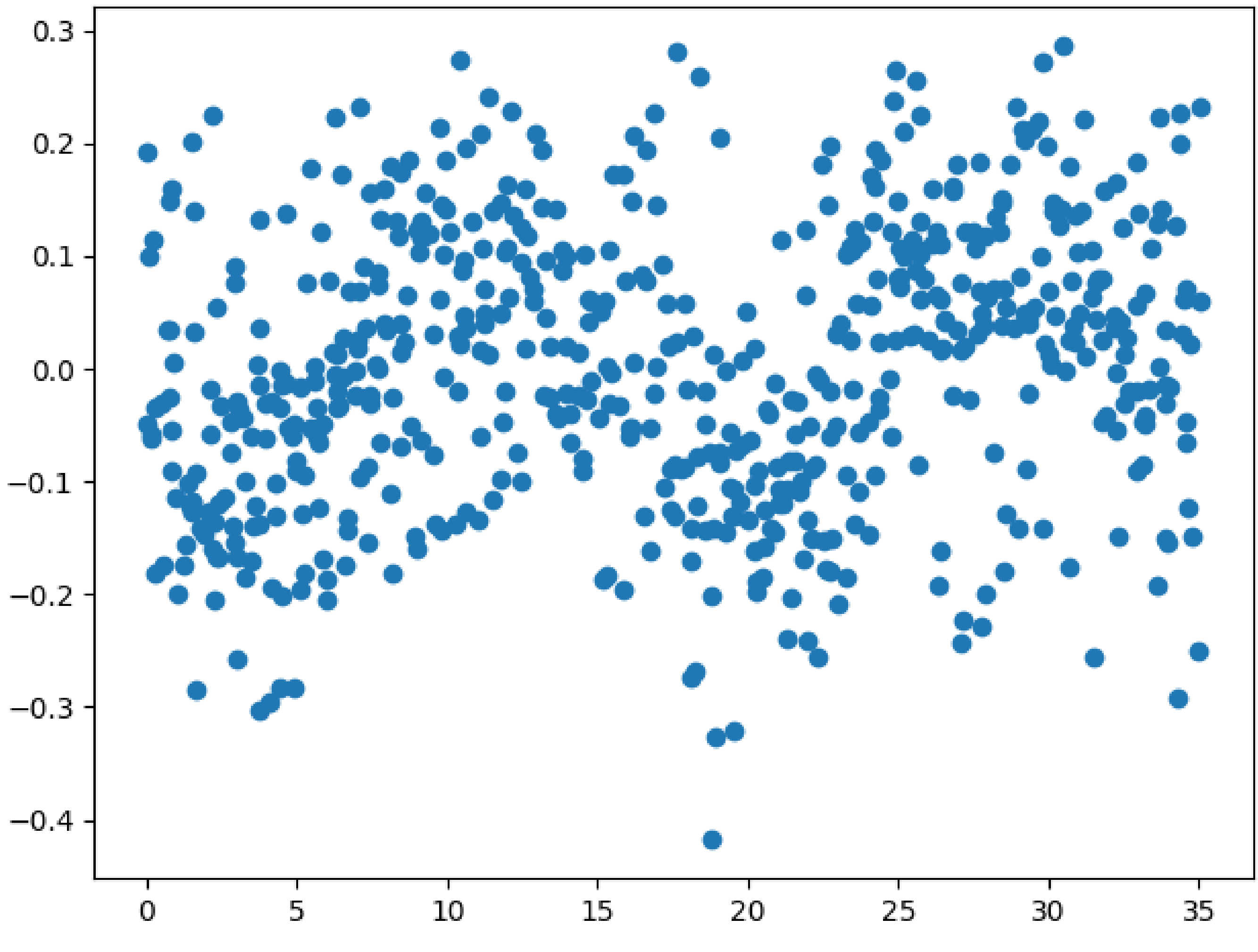

Figure 6: Same periodogram as displayed in Figure 4, but cropped into the region of interest: $P < 60\,\mathrm{s}$. The two distinct peaks occur at $P = 15.4\,\mathrm{s}$ and $P = 18.3\,\mathrm{s}$.

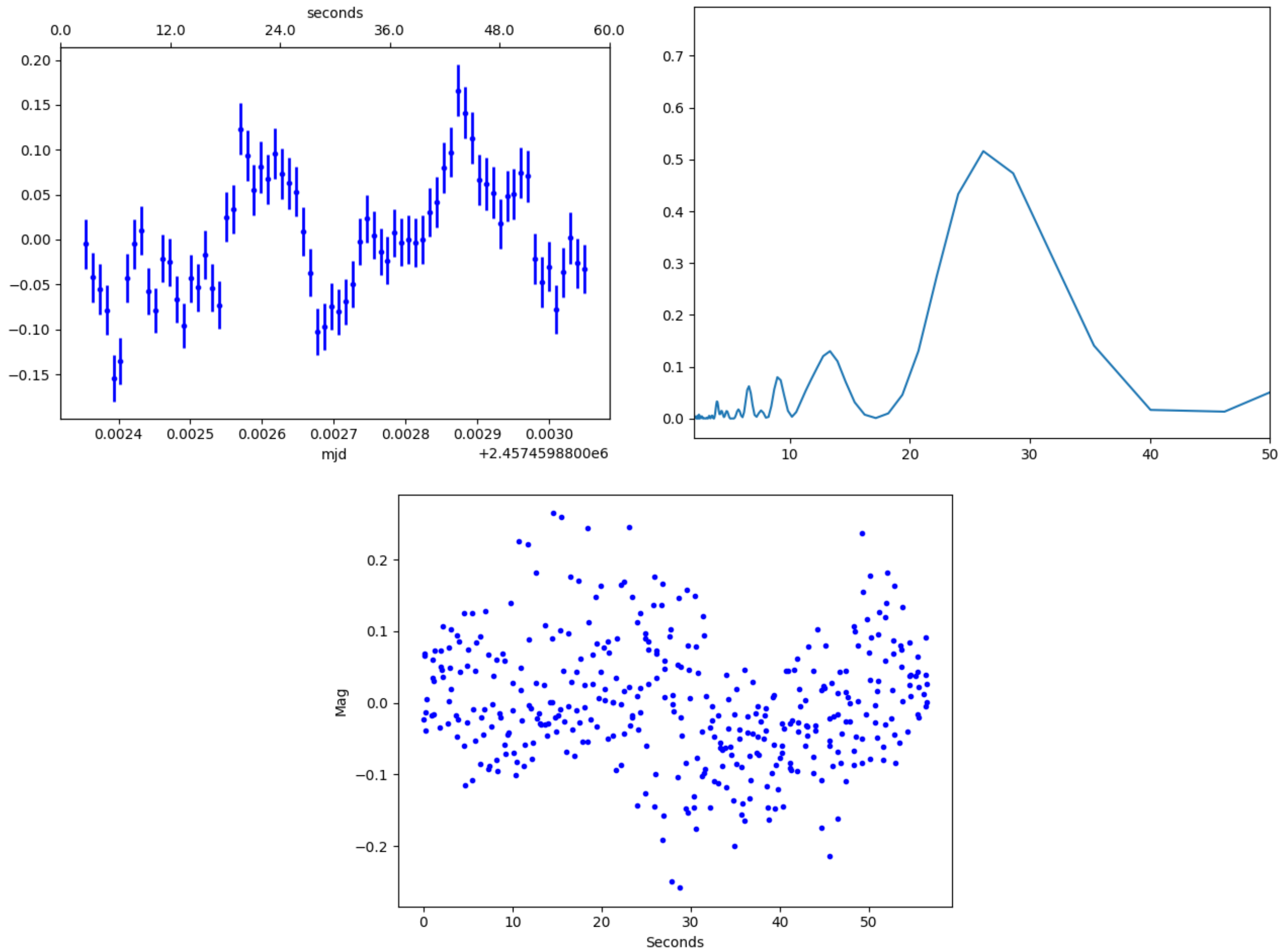

Lomb-Scargle periodogram for 2016 EV_{84} from **??**.
Lightcurve of 2016 EV_{84} folded on its dominant period of 57.2 seconds.

Figure 7: Lightcurve of 2016 EV_{84}, calculated from one exposure.
Lomb-Scargle periodogram for 2016 EV_{84} from **??**.
Lightcurve of 2016 EV_{84} folded on its dominant period of 57.2 seconds.

object	H	a [au]	e	i [deg]	time range [minutes]	RA range [deg]	Dec range [deg]	total exp.time [s]	obs	g obs	r obs	i obs	MegaCam chip
2015 TG24	26.7	0.75	0.44	3.98	29.7	0.29	0.05	360	6	2	2	2	31
2015 VH1	27.4	1.66	0.39	1.14	4849.8	9.51	1.44	780	13	5	4	4	31 & 22
2015 VH65	27.7	0.85	0.23	13.43	44.2	0.07	0.14	300	5	2	1	2	31 & 22
2015 VR64	27.4	1.49	0.38	1.53	46.9	0.40	0.01	480	8	6	2	0	22
2015 XA169	27.4	1.60	0.41	12.18	30.5	0.08	0.09	360	6	2	2	2	13
2015 XD169	26.9	1.08	0.12	3.79	60.6	0.07	0.07	720	12	4	4	4	22
2015 XN55	27.2	1.21	0.25	3.18	30.8	0.00	0.04	360	6	2	2	2	13
2015 XR169	28.7	1.20	0.34	0.04	60.0	0.29	0.14	720	12	4	4	4	4
2015 XV1	26.9	2.35	0.62	5.25	3276.3	9.79	6.25	720	12	4	4	4	13 & 22
2015 XY261	27.2	1.51	0.47	1.22	30.9	0.01	0.09	360	6	2	2	2	13
2015 YA	27.4	1.00	0.28	1.64	30.9	0.04	0.00	360	6	2	2	2	13
2016 AN9	26.8	1.94	0.50	8.04	5.8	0.01	0.01	120	2	2	0	0	3
2016 BA15	26.8	1.54	0.55	1.51	29.1	0.00	0.39	360	6	2	2	2	23
2016 CD137	26.1	1.08	0.23	4.63	29.3	0.00	0.06	360	6	2	2	2	22
2016 CD31	26.9	1.04	0.45	0.47	29.1	0.22	0.09	360	6	2	2	2	22
2016 CE194	26.1	1.95	0.52	1.85	29.1	0.03	0.03	1080	18	6	6	6	22 & 4
2016 CE3	18.4	2.58	0.11	2.93	28.8	0.55	0.07	360	6	2	2	2	22
2016 CG18	28.5	1.06	0.12	5.31	29.3	0.16	0.19	360	6	2	2	2	13
2016 CK31	27.1	1.32	0.29	6.88	29.3	0.24	0.06	720	12	4	4	4	13 & 4
2016 CW30	26.7	1.47	0.46	0.97	29.3	0.33	0.01	360	6	2	2	2	13
2016 EL157	27.1	1.95	0.53	7.19	29.2	0.04	0.06	360	6	2	2	2	13
2016 EN156	27.8	1.31	0.30	3.75	30.5	0.04	0.05	360	6	2	2	2	13
2016 EU84	29	0.92	0.10	3.35	29.4	0.04	0.01	720	12	4	4	4	13 & 4
2016 EV84	26.7	0.87	0.18	13.62	29.3	0.08	0.01	360	6	2	2	2	13 &22
2016 FF14	27.1	1.75	0.49	1.35	36.8	0.02	0.05	420	7	2	2	3	13
2016 GE1	26.7	2.10	0.53	10.77	36.8	0.09	0.15	420	7	2	3	2	13
2016 GG1	26.6	1.61	0.36	6.21	35.1	0.05	0.04	720	12	4	4	4	13 & 22
2016 HD3	28	0.91	0.24	0.60	29.1	0.07	0.06	360	6	2	2	2	13 & 22
2016 JB	27.1	0.91	0.14	9.69	29.1	0.03	0.11	360	6	2	2	2	13 & 4
2016 LT1	29	1.40	0.32	4.18	3822.8	16.43	8.15	720	12	4	4	4	4 & 13 & 22
2016 NM15	27.5	1.23	0.17	1.91	29.0	0.04	0.05	360	6	2	2	2	4 & 13 & 22